Journal of Fluids and Structures 66 (2016) 207–228

Contents lists available at ScienceDirect

Journal of Fluids and Structures

journal homepage: www.elsevier.com/locate/jfs

Aeroelastic simulations of stores in weapon bays using Detached-Eddy Simulation

S.V. Babu [c], G.J.M. Loupy [a], F. Dehaeze [c], G.N. Barakos [a,*], N.J. Taylor [b]

[a] CFD Laboratory, School of Engineering, University of Glasgow, Glasgow G12 8QQ, Scotland, UK
[b] MBDA UK Ltd, Filton, Bristol BS34 7QW, UK
[c] School of Engineering, University of Liverpool, Liverpool L69 3GH, UK

ARTICLE INFO

Article history:
Received 29 February 2016
Received in revised form
16 June 2016
Accepted 20 July 2016

Keywords:
Cavity flow
Store
Aeroelasticity
Transonic

ABSTRACT

Detached-Eddy Simulations of flows in weapon bays with a generic store at different positions in the cavity and with flexible fins are presented in this paper. Simulations were carried out to better understand the fluid–structure interactions of the unsteady, turbulent flow and the store. Mach and Reynolds numbers (based on the missile diameter) were 0.85 and 326.000 respectively. Spectral analysis showed few differences in the frequency content in the cavity between the store with rigid and flexible fins. However, a large effect of the store position was seen. When the store was placed inside the cavity, the noise reduction reached 7 dB close to the cavity ceiling. The closer the store to the carriage position, the more coherent and quieter was the cavity. To perform a more realistic simulation, a gap of 0.3% of the store diameter was introduced between the fin root and the body of the store. Store loads showed little differences between the rigid and flexible fins when the store was inside and outside the cavity. With the store at the shear layer, the flexible fins were seen to have a reduction in loads with large fluctuations in position about a mean. Fin-tip displacements of the store inside the cavity were of the range of 0.2% of the store diameter, and in the range of 1–2% of store diameter when at the shear layer.

1. Introduction

Modern military aircraft and Unmanned Combat Air Vehicles (UCAVs) employ internal weapon bays for stealth. During flight when weapon bay doors are open, the flow inside the bay is characterized by strong acoustics, unsteadiness and turbulence. These characteristics vary depending on the geometry of the bay, the flow regimes to which they were subjected, and the presence of stores. Shallow cavities can give rise to large loads and pitching moments on the store while deep cavities can give rise to large levels of fluctuating pressure. During carriage, a store and its control surfaces (canards, wings or fins) may undergo deformations that are tightly coupled to the flow inside the bay. This is where the versatility of Computational Fluid Dynamics (CFD) can aid the design and analysis of real stores in weapon bays.

Lawson and Barakos (2011) provide an extensive review of the experimental and numerical studies undertaken for clean cavity flows. While several studies have investigated clean cavity flow, only two (Coley, 2011; Finney, 2010) have included a

* Corresponding author.
E-mail addresses: savio.svb@gmail.com (S.V. Babu), g.loupy.1@research.gla.ac.uk (G.J.M. Loupy), florentdehaeze@free.fr (F. Dehaeze), george.barakos@glasgow.ac.uk (G.N. Barakos), nigel.j.taylor@mbda.co.uk (N.J. Taylor).

http://dx.doi.org/10.1016/j.jfluidstructs.2016.07.014
0889-9746/

Nomenclature

Latin

A_{ref}	reference area
C_l, C_m, C_n	rolling, pitching and yawing moment coefficient
C_X, C_Y, C_Z	axial, side and normal force coefficient
d	distance to the nearest wall
D	cavity depth
D_{mis}	missile diameter
$d\vec{x}$	displacement vector of the point $\vec{x}$
$d\vec{x}_1$, $d\vec{x}_2$, $d\vec{x}_3$, $d\vec{x}_4$	displacement vectors of the face four corners
$\mathbf{f}$	external force applied to the fin projected at every structural point
F	force
F, G, H	spatial flux vectors in Navier–Stokes equations
i	inviscid term
L	cavity length
M	moment
M_{inf}	freestream Mach number
n_m	number of eigenmodes
Q	unsteady terms in Navier–Stokes equations
Re	Reynolds number
Re_D	Reynolds number based on store diameter
s_1,s_2,s_3,s_4	stretching functions, defined in Eq. (18)
$\vec{S}$	source vector in Navier–Stokes equations
v	viscous term
W	cavity width
$\vec{x}_1$, $\vec{x}_2$, $\vec{x}_3$, $\vec{x}_4$	coordinates of the four face corners
x, y, z	Cartesian coordinates

Greek

α	modal amplitude
ϕ	fin shape
ϕ_i	eigenvector
ϕ_0	undeformed eigenvector
ϕ_1^0,ϕ_2^0	blending functions in the η-direction
ψ_1^0,ψ_2^0	blending functions in the ξ-direction
ρ_∞	freestream density
ξ,η	local coordinates on a block face
ω	eigenpulsation
ζ	structural damping coefficient

Acronyms

BISPL	Band-Integrated Sound-Pressure Level
CAA	Computational Aero Acoustics
CFD	Computational Fluid Dynamics
CSD	Computational Structural Dynamics
CVT	Constant Volume Tetrahedron
DES	Detached-Eddy Simulation
DG	Density Gradient
DNS	Direct Numerical Simulation
FEM	Finite Element Method
FFT	Fast Fourier Transforms
HMB	Helicopter Multi-Block
HPC	High Performance Computing
LES	Large-Eddy Simulation
MEM	Maximum Entropy Method
MUSCL	Monotone Upwind Schemes for Scalar Conservation Laws
OASPL	Overall Sound-Pressure Level
PSD	Power Spectral Density
RANS	Reynolds-averaged Navier–Stokes
S–A	Spalart–Allamaras
SAM	Spring Analogy Method
SPL	Sound-Pressure Level
TFI	Trans-Finite Interpolation
UCAV	Unmanned Combat Air Vehicle

store and for these cases, the store was assumed to be rigid. Until very recently, no literature was available on the topic of aeroelasticity of stores in cavities. Arunajatesan et al. (2013) presented initial results on a loosely coupled fluid structure interaction (FSI) framework to study the effects of the unsteady loads on the store and its components. The store had a length of 0.17 m and a diameter of 1.2 cm and was placed at carriage. They found that the maximum fin displacement was about 0.2% of the store diameter. Experimental work (Wagner et al., 2013, 2015) conducted to accompany the FSI framework used a cylindrical store installed in a cavity of $L/D=3.33$ and $L/W=1$. The store was found to significantly alter the cavity acoustics and responded to the flow at its natural structural frequencies. An early version of this work had been presented at the AIAA SciTech conference 2014 (Babu et al., 2014).

The current work employs Detached-Eddy Simulation (DES) with the Spalart and Allmaras (1994) turbulence model and a tightly coupled aeroelastic method to study the effect of flexible fins on the aerodynamic loads acting on a store at different positions relative to a weapon bay idealized as a rectangular cavity of $L/D=7$ and $W/D=2$. The simulations have been carried out at a Mach number of 0.85 and at a Reynolds number of 326.000 (based on the store diameter). A 0.5 mm gap between the root of the fins and the body of the store equivalent to 0.3% of the store diameter was introduced allowing root displacements and a more realistic geometry. Although DES results for the $L/D=7$ cavity were not validated for this study, due to lack of experimental results, past work (Lawson and Barakos, 2010, 2011) at the University of Liverpool used the Helicopter Multi-Block (HMB2) (Jarkowski et al., 2014) flow solver for cavities of $L/D=5$ and validated the method against experimental results for the M219 clean cavity (Nightingale et al., 2005) and a UCAV. Furthermore, the aeroelastic method was validated in past work (Dehaeze and Barakos, 2012) for the UH-60A rotor in forward flight.

The paper is organized as follows: A description of the flow solver used for the computations is presented in Section 2. The fluid structure interaction and the methodology to deform the fins of the store, through a tight coupling of the CFD and

CSD solvers, are explained in Section 3. The geometry of the store model and the structure multi-block topology are presented and discussed in Section 4. Section 5 explains the post-processing methods used for the presentation of the results. Section 6 presents and discusses the results from which conclusions are drawn and summarized in Section 7.

2. Flow solver

2.1. Governing equations

HMB2 (Barakos et al., 2005), which is of third order accuracy, solves the three-dimensional, unsteady, compressible Navier–Stokes equations on multi-block structured grids. The governing equations are the unsteady three-dimensional compressible Navier–Stokes equations, written in dimensionless form as:

$$\frac{\partial Q}{\partial t}+\frac{\partial}{\partial x}\left(F^i+\frac{1}{Re}F^v\right)+\frac{\partial}{\partial y}\left(G^i+\frac{1}{Re}G^v\right)+\frac{\partial}{\partial z}\left(H^i+\frac{1}{Re}H^v\right)=0$$

where Q contains the unsteady terms and F, G and H are spatial flux vectors, split into their inviscid (i) and viscous (v) parts. The code solves the governing equations on multi-block structured grids using a cell-centered finite volume method. The convective terms are discretized using either Osher and Chakravarthy's (1983) or Roe's (1981) scheme. Monotone Upwind Schemes for Scalar Conservation Laws (MUSCL) interpolation (Leer, 1974) is used to provide formally third order accuracy and the van Albada et al. (1982) limiter is used to avoid spurious oscillations across shocks. An implicit, dual step method (Jameson, 1991) is used for time-marching and the final algebraic system of equations is solved using a conjugate gradient method. A number of turbulence models including one and two-equation statistical models as well as Large-Eddy Simulation (LES) and DES have been implemented into the code. More details of the employed CFD solver and turbulence models are given in Jarkowski et al. (2014). For the work presented in this paper, DES was employed along with the Spalart–Allamaras turbulence model (Spalart and Allmaras, 1994).

2.2. Detached-Eddy Simulation

Despite the potential of LES, there are problems in resolving the near-wall turbulent stresses since the required resources approach those of Direct Numerical Simulation (DNS). Pure LES gives about 10 times higher Reynolds numbers than DNS but is of limited application for the flow at hand. While RANS is an option, alternatives exist involving hybrids of LES and RANS such as DES. The original idea of DES was postulated by Spalart and Allmaras (1994). Its underlying principle involved using RANS for the near-wall and boundary layer and LES everywhere outside. Spalart modified the S–A model to achieve a DES equivalent. The wall distance (d) is now recomputed according to the DES principle and represented by $\tilde{d}$. In the pure one-equation S–A turbulence model, the terms $\tilde{d}$ and d are identical. However, the DES formulation of $\tilde{d}$ is given by:

$$\tilde{d}=C_{DES}\Delta \tag{1}$$

where C_{DES} is a constant and Δ is the metric of the grid size.

In practice, the distance to the wall in the DES formulation of the one-equation S–A model is expressed as a comparison between the actual distance to the wall and that calculated by $C_{DES}\Delta$, which essentially computes the size of the maximum cell length:

$$\tilde{d}=\min\left(d,\, C_{DES}\Delta\right) \tag{2}$$

$$\Delta=\max\left(\Delta_x,\,\Delta_y,\,\Delta_z\right)\quad \forall \text{ cell.} \tag{3}$$

When the cell length ($C_{DES}\Delta$) is less than the actual distance to the nearest wall (d), LES is triggered. RANS is activated when the converse occurs. This boundary between LES and RANS is therefore completely dependent on the geometry and on the density of the computational mesh. Note that other metric relations are also possible.

3. Fluid–structure interaction

To compute the deformation of the fins, a modal approach was chosen where the fin deformation was expressed as a function of eigenmodes. A Nastran Finite Element Model (FEM) of the fin, made of 240 000, CTETRA (M.S. Corporation), triangular mesh elements was used to obtain the eigenmode shapes and frequencies using Nastran (M.S. Corporation) through a nonlinear static calculation (SOL 106, M.S. Corporation). The mode type and the frequencies of the first four fin with gap modes are shown in Table 1. The fins shape, ϕ, is obtained as the sum of the undeformed eigenvector ϕ_0 and the sum of the eigenvectors, ϕ_i, that represent the displacement for each mode multiplied by the corresponding modal amplitude, α_i:

Table 1
Mode type and frequencies for the first four structural modes of the fin. The first four Rossiter modes (Rossiter, 1964) for a cavity length of 3.33 m are also shown for comparison.

Mode	Mode type	Structural mode (Hz)	Rossiter mode (Hz)
1	Bending + twisting	144.1	25.5
2	In-plane bending	158.1	59.6
3	Twisting	232.0	93.6
4	Bending	923.5	127.6

$$\phi = \phi_0 + \sum_{i=0}^{n_m} \alpha_i \phi_i \tag{4}$$

where n_m is the number of eigenmodes. Knowing the eigenvectors, ϕ_i, the modal amplitude, α_i, is obtained at every step of the CFD method by solving the differential equation:

$$\frac{\partial^2 \alpha_i}{\partial t^2} + 2\zeta_i \omega_i \frac{\partial \alpha_i}{\partial t} + \omega_i^2 \alpha_i = \mathbf{f}.\ \phi_i \tag{5}$$

where $\mathbf{f}$ is the aerodynamic load, ω_i is the eigenpulsation frequency and ζ_i is the damping coefficient. The modal representation of the structure allows for tight coupling between the flow and structural solutions with the shape of the mesh and the aerodynamics loads computed and exchanged at every sub-iteration of the employed dual time-step method.

Rossiter's modes are associated with the movement of the shear layer at the lip of the cavity as well as the movement of large flow structures inside the cavity. It may be possible that flow structures moving with Rossiter's frequencies could lead to fluid dynamic forcing if some of the forcing these structures generate on the fins may be strong enough to excite the structure.

The flow computation was initiated by keeping the fins rigid and allowing the solution to converge. Once convergence of the store aerodynamic loads was obtained, the aeroelastic simulation was initiated by applying the aerodynamic loads calculated from the fluid grid onto the surface of each fin, allowing them to oscillate freely.

To create a stable transition from a rigid state to an oscillating state, the aeroelastic computation began with a strong damping coefficient, $\zeta = 0.7$. This dampened the oscillations that arose from the sudden change in forcing applied to the system. As the flow converged, the damping coefficient was gradually lowered to 0.1, which allowed the deformation to develop.

The tight coupling between the CFD and CSD domains requires the association of the nodes on the structural model to the nodes in the fluid mesh and vice-versa. The difference in resolution between the structural and fluid domain requires interpolation of the structural solution onto the surface of the fin in the fluid domains. This problem was addressed and documented by Dehaeze and Barakos (2012) who amongst others used a hybrid technique for the deformation of the CFD mesh of a rotor blade, according to its structural model, while maintaining the mesh quality. The deformation technique is carried out in three stages through the use of a Constant Volume Tetrahedron (CVT) method, a Spring Analogy Method (SAM) and a Trans-Finite Interpolation (TFI). CVT is first used to interpolate the deformed shape of the fin surface, following which, the vertices of the blocks are moved by the spring analogy method and finally the entire mesh is regenerated using TFI (Dehaeze and Barakos, 2012).

3.1. Constant Volume Tetrahedron

CVT is used for the exchange of information between the fluid and structural domains by projecting each fluid point to the nearest triangular structural element such that the fluid point moves linearly with the structural element while conserving the volume bound by the tetrahedron, formed by the coordinates of the triangular structural element and the fluid point (Dehaeze and Barakos, 2012).

3.2. Spring Analogy Method

Once the new positions of the fluid points are obtained, SAM is used to update the positions of the block vertices before it is regenerated using TFI. Fig. 1(b) shows the springs that are applied on each edge and diagonal of the first two layers of blocks around the fin, i.e. the first layer of blocks that is in direct contact with the fin and the immediate layer of blocks after. The springs on the edges of the block avoid large compression and expansion of the block faces while the springs on the block diagonals limit the skewness of the cells. Controlling the skewness of the cells is particularly important in areas close to solid surfaces where there is a refinement of cells with an exponential distribution. If the skewness is not controlled in these regions, even moderate deformations can lead to poor mesh quality or folding of cells giving rise to negative volumes in the block. In this way, SAM allows for large deformations while maintaining high mesh quality (Dehaeze and Barakos, 2012).

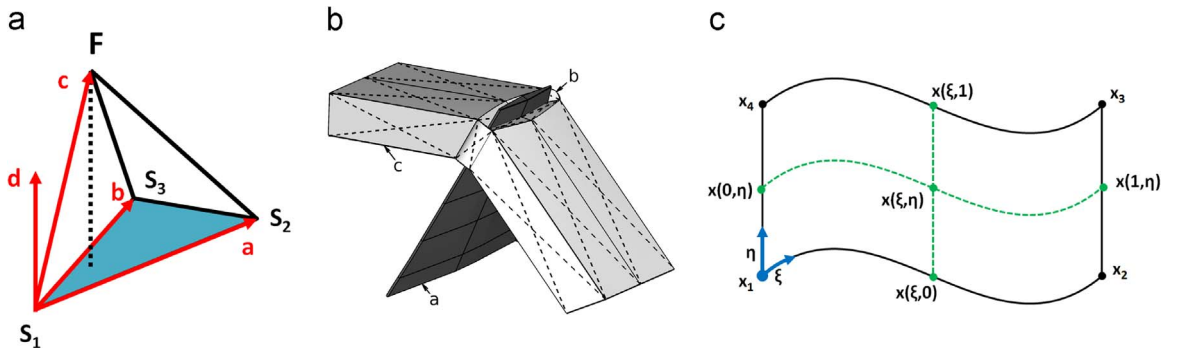

Fig. 1. Methods used for the deformation of the fin surface(a) Projection of a point from the fluid grid (F) to a structural element (S1, S2, S3) (b) SAM, a: solid fin surface, b: first layer of blocks and c: second layer of blocks around the fin (c) TFI application on a.

3.3. Trans-Finite Interpolation

TFI is used, finally, to interpolate the block face deformation from the edge deformations and then the full block deformation from the deformation of the block faces. The mesh deformation uses a weighted approach to interpolate a face/block from the boundary vertices/surfaces respectively. The weight depends on the curvilinear coordinate divided by the length of the curve for which the notation is shown in Fig. 1(c). The generation of the mesh on a block face ($\vec{x_1}$, $\vec{x_2}$, $\vec{x_3}$, $\vec{x_4}$) can be expressed as:

$$d\vec{x}(\xi,\eta) = \vec{f_1}(\xi,\eta) + \phi_1^0(\eta)[d\vec{x_1}(\xi) - \vec{f_1}(\xi,0)] + \phi_2^0(\eta)[d\vec{x_3}(\xi) - \vec{f_1}(\xi,1)], \tag{6}$$

where $\vec{f_1}$ is defined as:

$$\vec{f_1}(\xi,\eta) = \psi_1^0(\xi)d\vec{x_4}(\eta) + \psi_2^0(\xi)d\vec{x_2}(\eta), \tag{7}$$

with $d\vec{x_1}$, $d\vec{x_2}$, $d\vec{x_3}$ and $d\vec{x_4}$ representing the displacements of the four faces corners and ϕ and ψ representing the blending functions in the η and ξ directions. The blending functions are expressed as a function of the stretching functions s_1, s_2, s_3 and s_4:

$$\psi_1^0(\eta) = 1 - s_1(\xi) \tag{8}$$

$$\psi_2^0(\eta) = s_3(\xi) \tag{9}$$

$$\phi_1^0(\eta) = 1 - s_4(\eta) \tag{10}$$

$$\phi_2^0(\eta) = s_2(\eta). \tag{11}$$

The stretching function s_1 is defined by:

$$s_1(\xi) = \frac{\widehat{x_1x(\xi,0)}}{\widehat{x_1x_2}}, \tag{12}$$

where $\widehat{x_1x_2}$ is the curvilinear length between $\vec{x_1}$ and $\vec{x_2}$. s_2, s_3 and s_4 are defined in a similar way for the curves x_2x_3, x_3x_4 and x_4x_1 respectively. The interpolation of the inside of the block from the shape of the block faces follows the same method (Dehaeze and Barakos, 2012).

4. Model geometry and mesh generation

The geometry and structured multi-block grids for all configurations reported herein were generated using ICEMCFD (ANSYS, 2014). An idealized rectangular cavity geometry was used that had L/D and W/D ratios of 7 and 2 respectively. This was then combined with the geometry of a generic four finned store provided by MBDA Missile Systems (Taylor, 2011). For all computations, the geometry was non-dimensionalized by the length of the cavity, $L = 3.33$ m.

For all configurations of the store and cavity, the store was oriented in a cross (X) configuration. The root of the fin was fixed on the body of the store with a gap of 0.5 mm equivalent to 0.3% of the store diameter was introduced (Fig. 3). The gap was resolved in 18 computational cells introduced between the root of the fin and the body. Table 2 lists the computational details including grid sizes for the different computations presented in this paper. The mesh size and the distribution of

Table 2
Details of the computations at carriage and the associated grids.

Computation details	Carriage		Shear layer		Outside cavity	
Method	Rigid	Aeroelastic	Rigid	Aeroelastic	Rigid	Aeroelastic
Grid size (10^6 cells)	28.5	28.5	30.5	30.5	35.0	35.0
Number of blocks	3208	3208	3678	3678	4474	4474
Processors	128	128	256	256	256	256
CFD time-step (10^{-5} s)	1.18	1.18	1.18	1.18	1.18	1.18
Unsteady tolerance	0.001	0.001	0.001	0.001	0.001	0.001
Number of time-steps	17 000	21 500	21 500	42 500	12 700	12 700
Signal duration (s)	0.20	0.25	0.25	0.5	0.15	0.15

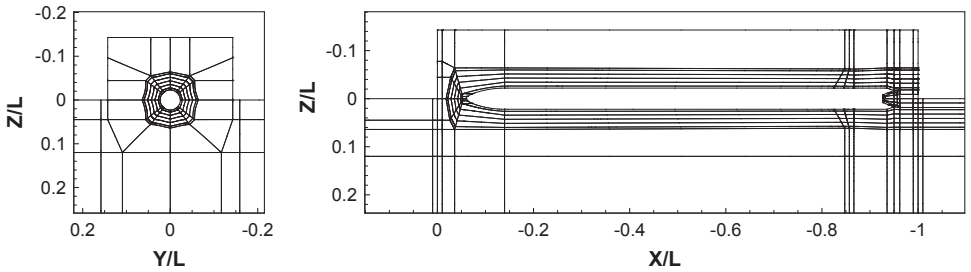

Fig. 2. Multi-block topology for the store at the shear layer of the cavity.

points were decided based on previous experience with cavity flow simulation (Nayyar, 2005; Lawson, 2009; Lawson and Barakos, 2010). The employed multi-bloc topology can be seen in Fig. 2.

Fig. 4 shows the store at three positions relative to the cavity used for the computations, these are: 1. inside the cavity at half the cavity depth, 2. at the cavity shear layer, and 3. outside the cavity at half the cavity depth from the shear layer. For all cases the store was positioned at the centerline of the cavity with its principal axis aligned with the lateral centerline of the cavity. The store was 3 m long such that the nose and base of the store were 0.165 m from the aft and front walls of the cavity respectively. The base diameter of the store was 0.153 m, giving it a fineness ratio of 19.5.

5. Post-processing methods

Transonic cavity flows are characterized by their highly unsteady and turbulent stochastic nature as well as strong acoustic emissions. This section presents the analysis techniques carried out on the unsteady data and the methods of flow visualization.

The CFD solver outputs flow-field files written at specific instances of time as specified by the user. In addition to this it also outputs data from specific 'probes' that are placed in the flow. The locations of the probes are defined at the beginning of the computation and are then written at every time step performed and are therefore sampled at a high enough frequency for spectral analyses.

5.1. Pressure signals

The Power Spectral Density (PSD), Overall Sound-Pressure Level (OASPL) and Band-Integrated Sound-Pressure Level (BISPL) are the basis of comparison for numerical unsteady pressure data along the cavity floor. The PSD is used to study the frequency content of a signal at a given location and is based upon the unsteady pressure p', where $p' = p - \overline{p}$. The PSD was calculated using the Burg estimator (Childers, 1978) (also known as Maximum Entropy Methods or MEM) as it produces better resolved peaks for short signals than traditional Fast Fourier Transforms (FFT) (Larcheveque et al., 2004). For a description of the PSD in terms of decibels (dB), the natural definition is that of the Sound-Pressure spectrum Level (SPL, Pierce, 1989):

$$SPL(f) = 10\mathrm{LOG}_{10}\left[\frac{PSD(f)\Delta f_{ref}}{p_{ref}^2}\right] \tag{13}$$

where Δf_{ref} is a reference frequency, usually set to 1 Hz and p_{ref} is the international standard for the minimum audible sound, which has the value of 2×10^{-5} Pa (Pierce, 1989).

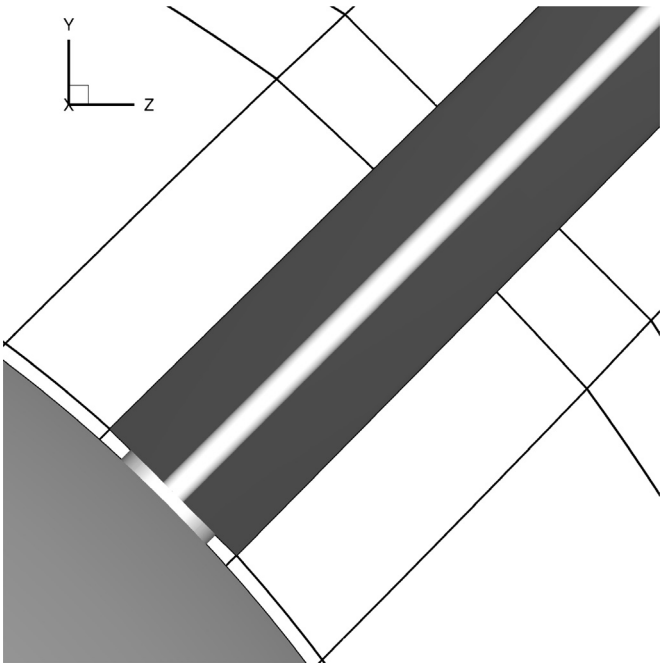

Fig. 3. Fin root detail.

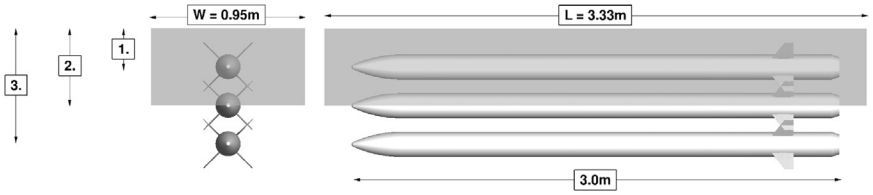

Fig. 4. Store positions relative to the bay for the three simulations. 1. Store at carriage position, 2. store at cavity shear layer, and 3. store at half-cavity-depth outside cavity.

The variation in pressure levels along the cavity floor was studied using the Root-Mean-Square (RMS) of the unsteady pressure, p'_{rms}. Although p'_{rms} is measured in Pascals (or any other unit of pressure), it is customary in cavity flow studies to report it as the Overall Sound-Pressure Level (OASPL, Pierce, 1989):

$$OASPL = 20\mathrm{LOG}_{10}\left[\frac{p'_{rms}}{p_{ref}}\right] \tag{14}$$

which has the units of decibels. BISPL plots show the energy content within a particular frequency range and are calculated using the following equation:

$$BISPL = 20\mathrm{LOG}_{10}\left[\left(\int_{f_1}^{f_2} PSD(f)\right)^{1/2}\cdot\frac{1}{p_{ref}}\right] \tag{15}$$

where f_1 and f_2 are the lower and upper limits of the desired frequency range. For cavity flow studies, the BISPL plots are centered around the first four Rossiter modes.

The tones in the PSD are usually termed Rossiter modes (Rossiter, 1964) and a semi-empirical formula is available for the estimation of their frequencies. Rossiter based the formula on experimental results over a range of Mach numbers from 0.4 to 1.4 and on various cavity aspect ratios. The modified version by Heller et al. (1971) is as follows:

$$f_m = \frac{U_\infty}{L}\left[\frac{m-\alpha}{M_\infty\left(1+\left(\frac{\gamma-1}{2}\right)M_\infty^2\right)^{-1/2}+1/\kappa_\nu}\right] \tag{16}$$

where f_m is the frequency of mode m, U_∞ is the free-stream velocity, M_∞ is the free-stream Mach number, L is the cavity length, γ is the ratio of specific heats, α represents a phase shift and κ_ν is a constant dependant on the cavity geometry and test conditions. These constants have the values 1.4, 0.25 and 0.57 respectively (Heller et al., 1971).

5.2. Loads

The loads on the complete store including the body and the fins are computed at the store gravity center placed at 50% of its length. The hinge moments on the fins alone are computed at the fin root. The force coefficients (C_{force}) and the moment coefficients (C_{moment}) are computed as:

$$C_{force} = \frac{F}{\frac{1}{2}\rho_\infty U_\infty^2 A_{ref}} \tag{17}$$

$$C_{moment} = \frac{M}{\frac{1}{2}\rho_\infty U_\infty^2 D_{mis} A_{ref}} \tag{18}$$

with F and M the force and moment and $A_{ref} = \pi D_{mis}^2/4$ the store reference area.

All loads computed on the store are presented in the right-handed North-East-Down (NED) axis system defined as x positive forward of the nose of the store, y positive right (viewed from the back of the store) and z positive down as shown in Fig. 5(a) where the axes are mutually orthogonal. The loads computed on each fin are presented in the local fin axis system. The fin axis system is defined as x positive forward, y positive outboard (from root-to-tip) and z completes the three axis set as seen in Fig. 5(b)–(e).

5.3. Mesh convergence

Since no experimental data is available for the previously described cases, some initial computations were performed at free-stream Mach number of 0.85 and Reynolds number based on the diameter of the store of 326.000. The store was placed at the carriage position. Two grids were used for these computations with the SAS model having 22 and 30 million points. The computations were run for 0.2 s and Fig. 6 compares the results.

The Overall Sound Pressure Level (OASPL) along the centerline of the cavity bottom is used. Both grids show the correct,

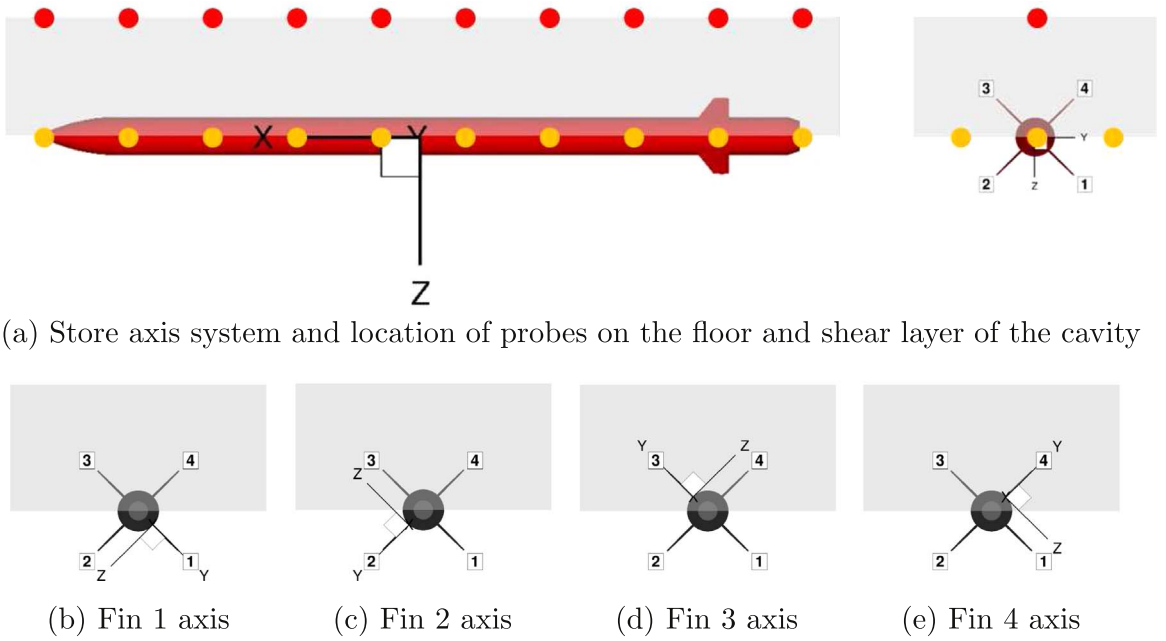

(a) Store axis system and location of probes on the floor and shear layer of the cavity

(b) Fin 1 axis (c) Fin 2 axis (d) Fin 3 axis (e) Fin 4 axis

Fig. 5. Store and fin axis systems. Red circles represent probes along the floor while orange circles represent probes along the shear layer of the cavity. (For interpretation of the references to color in this figure caption, the reader is referred to the web version of this paper.)

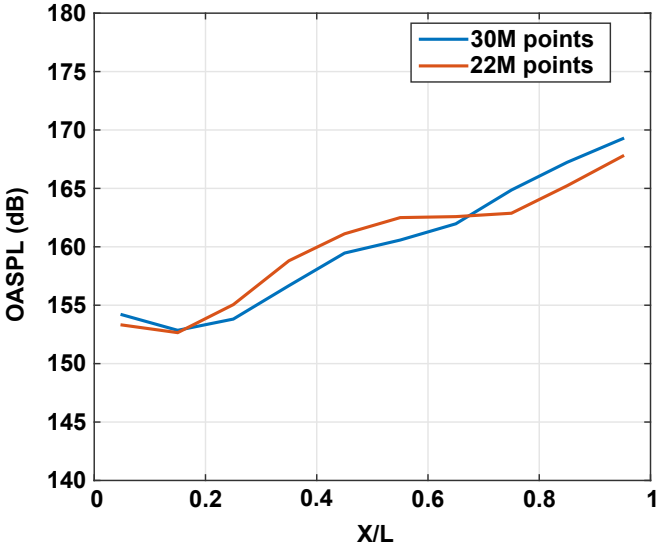

Fig. 6. Comparison of two levels of mesh refinement for the OASPL along the centerline of the cavity bottom.

tick-shaped distribution for a cavity case without doors characteristic of a strong cavity mode 1 (Lee, 2010). For computations where simulation of turbulence is used, the finer the mesh, the more of the flow spectrum is resolved, and so the differences between the two grids are considered to be small. For the rest of the paper, grids between 28 and 35 million cells were used.

6. Results and discussion

All computations (Table 2) presented in this paper were performed using two HPC facilities. First, the N8 HPC system, 'Polaris', located at Leeds University in the U.K. was used, where each node is composed of 8 cores of the Intel@ Xenon E5-2670 processor, that has a total of 5320 cores. The second was the Chadwick HPC system of the University of Liverpool that has a similar configuration to the N8 HPC system but with a third of the number of cores.

Rigid fin computations were performed for a store at each of the three positions relative to the cavity. Once the flow converged for these three computations, the same flow solutions were used as a starting point for the computations with aeroelastic fins. For all computations, a Mach number of 0.85 and Re_D of 326.000 was used. Although this Re_D may be lower than what a full-size configuration would experience, past work with cavities (Nayyar, 2005; Lawson, 2009) suggests that the dynamics of the cavity flow is not significantly affected. The lower Re_D was preferred here due to the economies it offers in terms of the mesh resolution and computing time required. Much the same way, the length of the computation was decided based on past experience so that the results could be obtained with the available computer resources. Longer signals would be preferable though here up to 0.5 s of flow time was computed. This was enough for the structure excitation to take pace and develop, as presented in the following paragraphs.

6.1. Averaged flow-field

In order to study the effect of a store on the cavity flow-field, time-averaged contours of Mach number were visualized using slices along and perpendicular to the lateral centerline (Fig. 7). The blockage introduced by the store at carriage made the shear layer more coherent and lowered the flow spillage over the sides of the cavity near the aft wall in comparison with the empty cavity.

When the store was placed at the shear layer, the blockage effect towards the aft of the cavity was reduced which increased the flow spillage over the sides of the cavity. The region of accelerated flow by the aft wall also increased compared to when the store was at carriage. Although the centerline of the cavity was directly affected by the presence of the store, the flow-field began to resemble the clean cavity flow-field in terms of the average Mach number field.

Outside the cavity, the store had little to no influence on the flow-field inside the cavity evidenced by the similarities between Figs. 7(a) and (g). The flow-field along the centerline resembles closely that of the clean cavity with some influence of the aft half of the store on the shear layer. Although the region past the aft wall is dissimilar to that of the clean cavity, due to the flow separating off the store, the overall flow-field is very similar to the clean cavity flow-field.

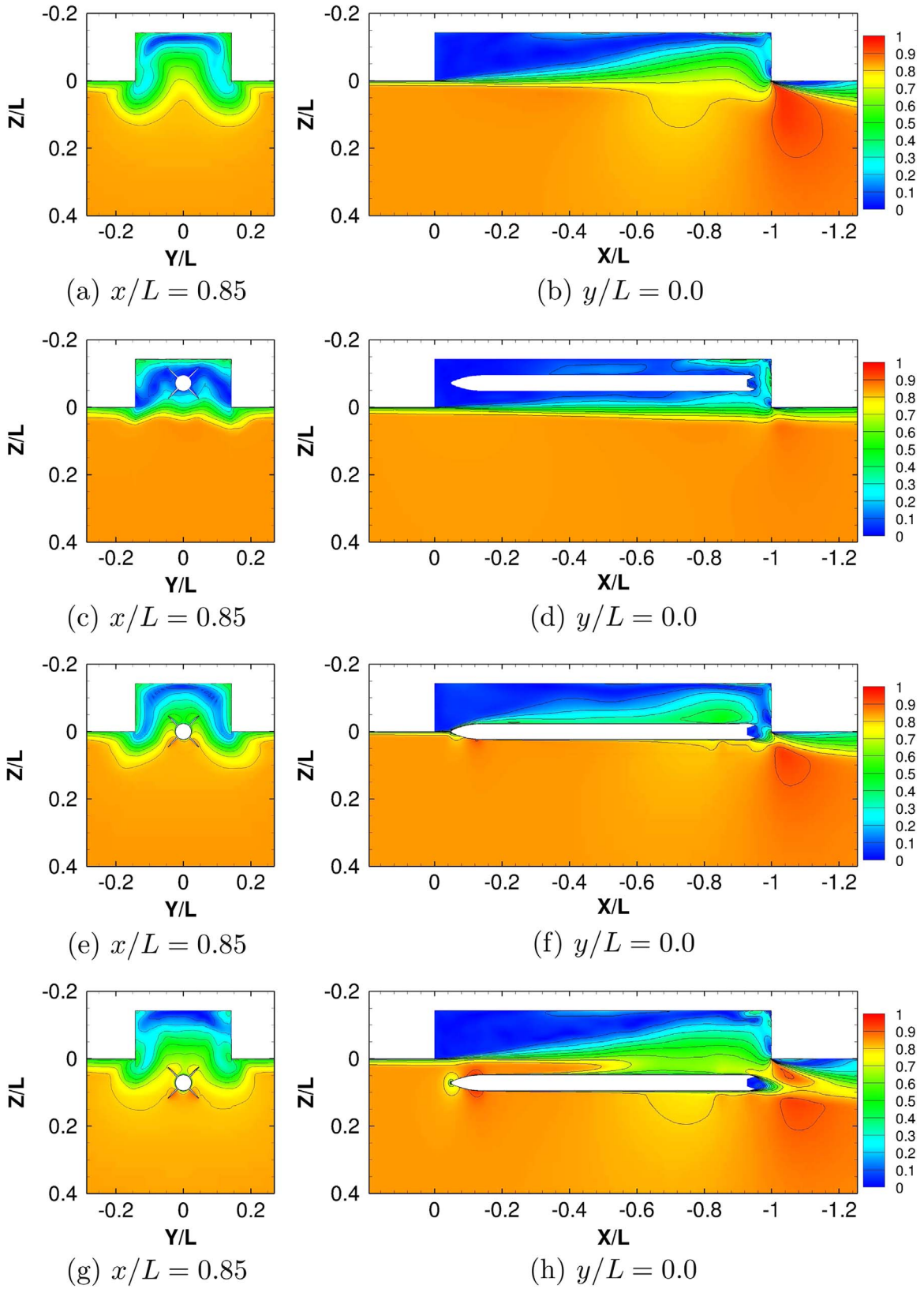

Fig. 7. Time-averaged contours of Mach number for the clean cavity (a) and (b) and, with a store at carriage (c) and (d), at the shear layer (e) and (f) and outside (g) and (h) x/L = 0.85, and y/L = 0.0.

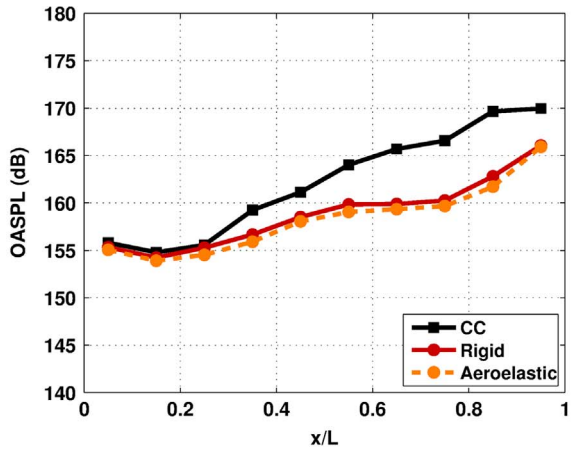

(a) Probes along the cavity floor, z/L=0.0

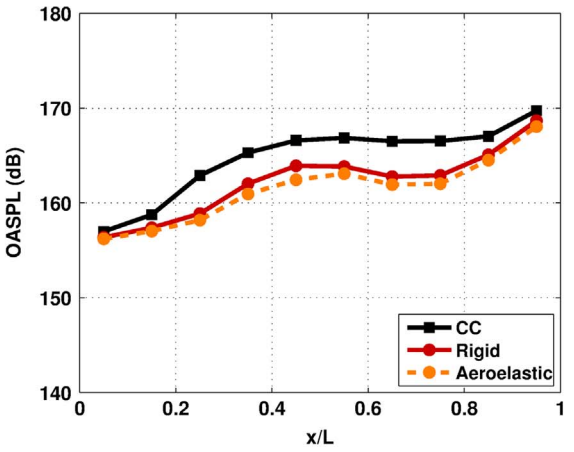

(b) Probes along the cavity shear layer

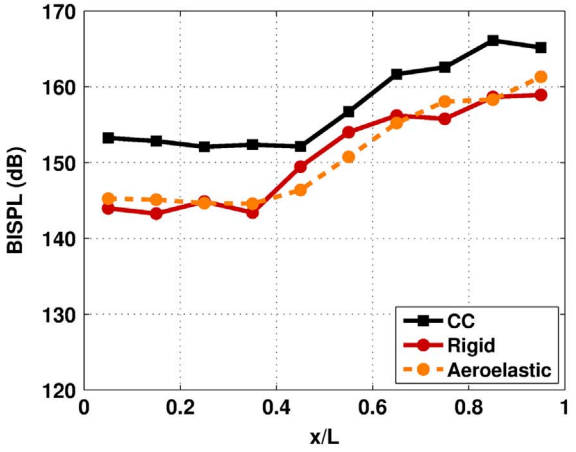

(c) Mode 1: $10 \leq f \leq 40$ Hz

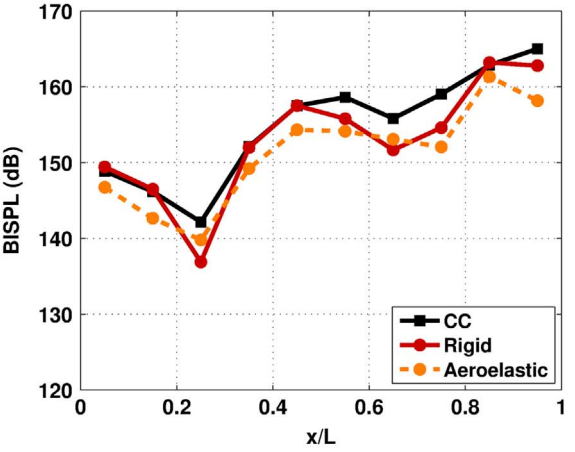

(d) Mode 2: $40 \leq f \leq 70$ Hz

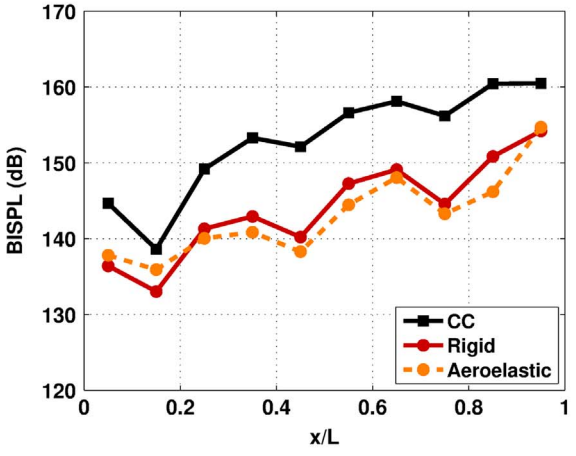

(e) Mode 3: $70 \leq f \leq 110$ Hz

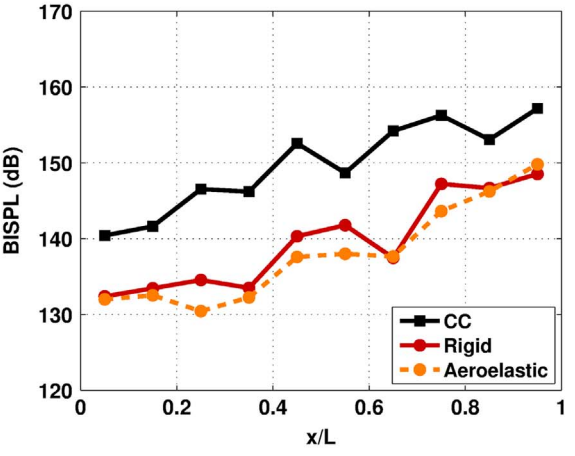

(f) Mode 4: $110 \leq f \leq 140$ Hz

Fig. 8. OASPL along the centerline of the cavity floor (a) and shear layer (b) and BISPL (c)–(f) plots along the centerline of the cavity floor for the store at carriage position. CC: clean cavity.

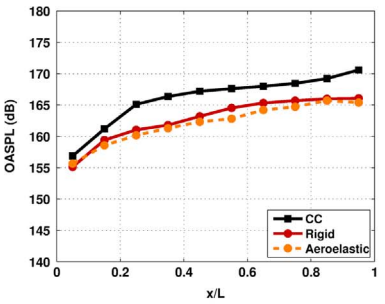

(a) Probes along the shear layer (port side of store)

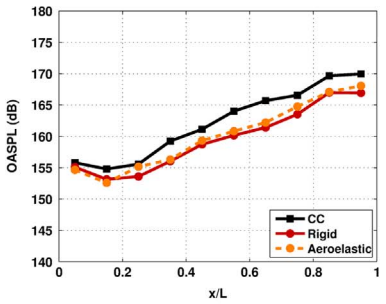

(b) Probes along the floor

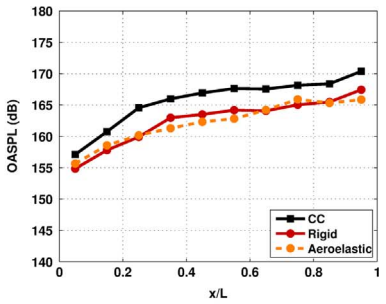

(c) Probes along the shear layer (starboard side of store)

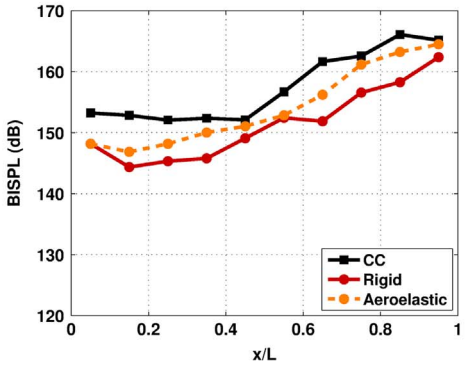

(d) Mode 1: $10 \leq f \leq 40$ Hz

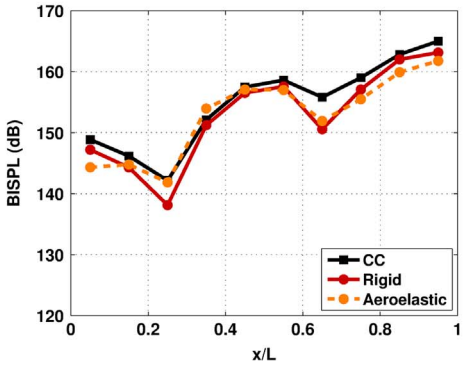

(e) Mode 2: $40 \leq f \leq 70$ Hz

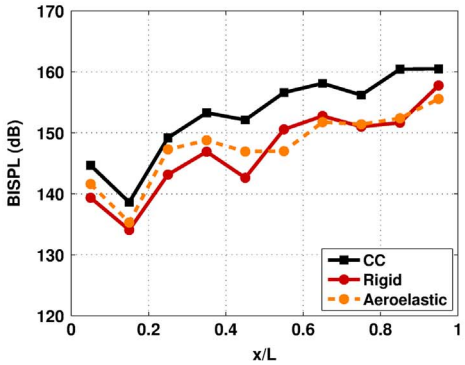

(f) Mode 3: $70 \leq f \leq 110$ Hz

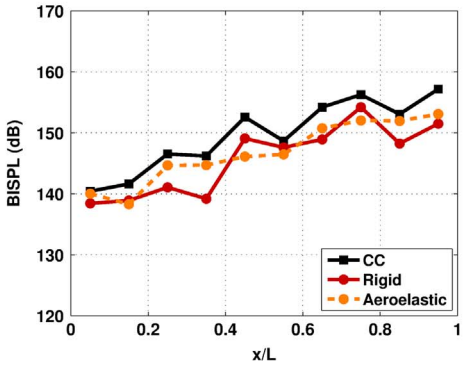

(g) Mode 4: $110 \leq f \leq 140$ Hz

Fig. 9. OASPL (a)–(c) and BISPL (d)–(g) plots along the centerline of the cavity floor for store at shear layer. CC: clean cavity.

6.2. Overall and banded sound pressure levels on cavity floor

OASPLs along the centerline of the floor of the cavity for the store at different positions relative to the cavity are shown in Figs. 8–10. When the store was positioned at carriage it was seen to pacify the flow compared to a clean case from about 30% of the cavity length to the aft wall. The BISPL shows that modes 1, 3 and 4 show the larger decrease, up to 10 dB for mode 4 (Fig. 8(f)). For the case of the store at the shear layer, the OASPL was more evenly distributed throughout the length of the cavity and closer to the clean cavity (Fig. 9). The BISPL plot shows that all modes were closer to the clean cavity. OASPL and BISPL plots for the store outside the cavity showed that there was little effect on the cavity acoustics compared to the clean cavity. Negligible differences were seen, except for the mode 1 that reached a difference of 5 dB at the aft wall.

This suggests that the store has a pacifying effect on the cavity flow. This may be due to the presence of the store in the bay that modifies the flow topology (Fig. 7) and consequently also the cavity acoustics. The quieter cavity flow for the store at carriage may be caused by the shear layer that is seen not to go deep in the cavity (Fig. 7(d)). This may

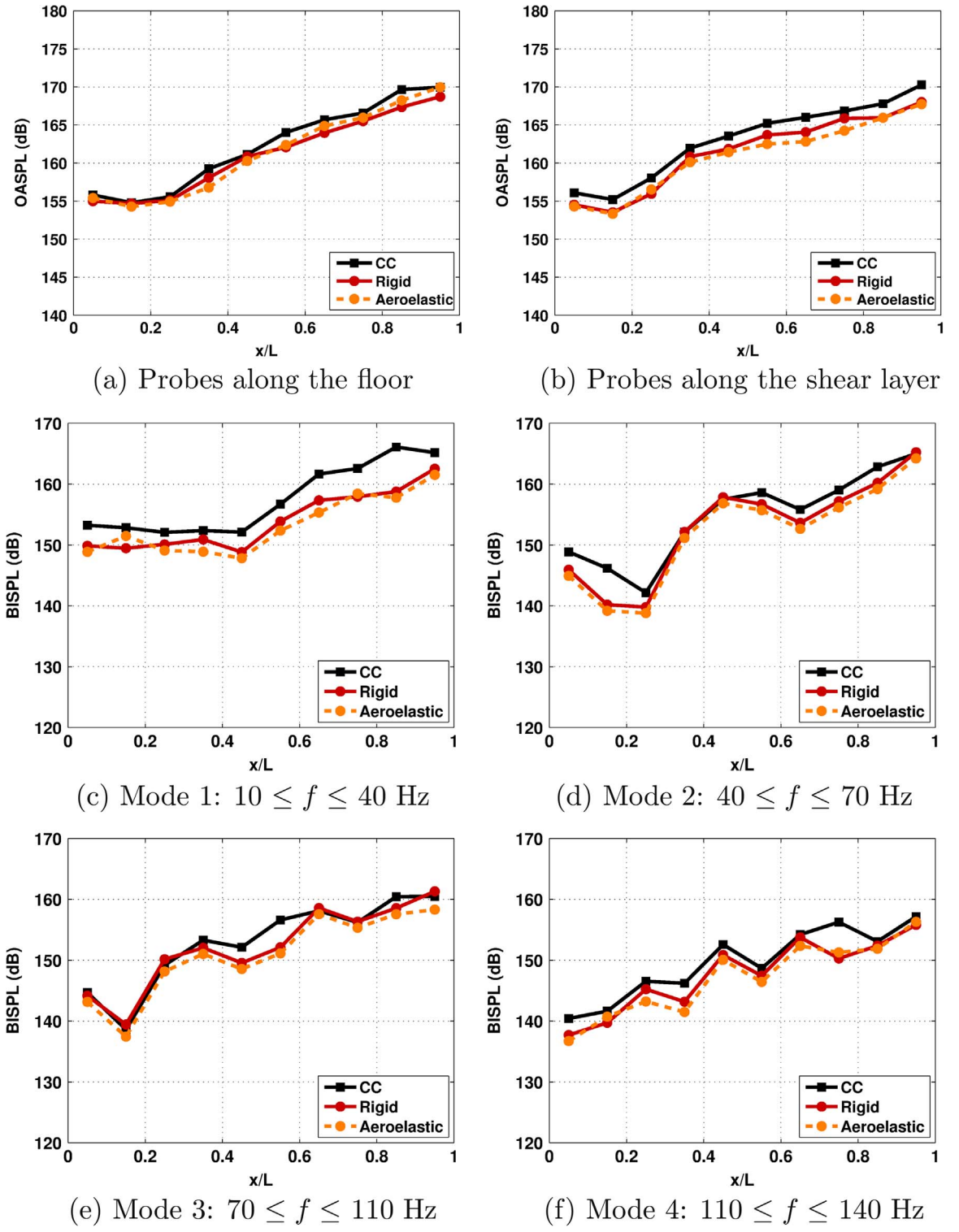

Fig. 10. OASPL (a) and (b) and BISPL (c)–(f) plots along the centerline of the cavity floor for store outside the cavity. Results from the clean cavity and cavity with store are shown.

weaken the cavity resonance.

The aeroelasticity did not cause noticeable effect on the BISPL and the OASPL compared to the store position effect. It may be due to limitation of the aeroelasticity to the fins and the small displacements of the fins.

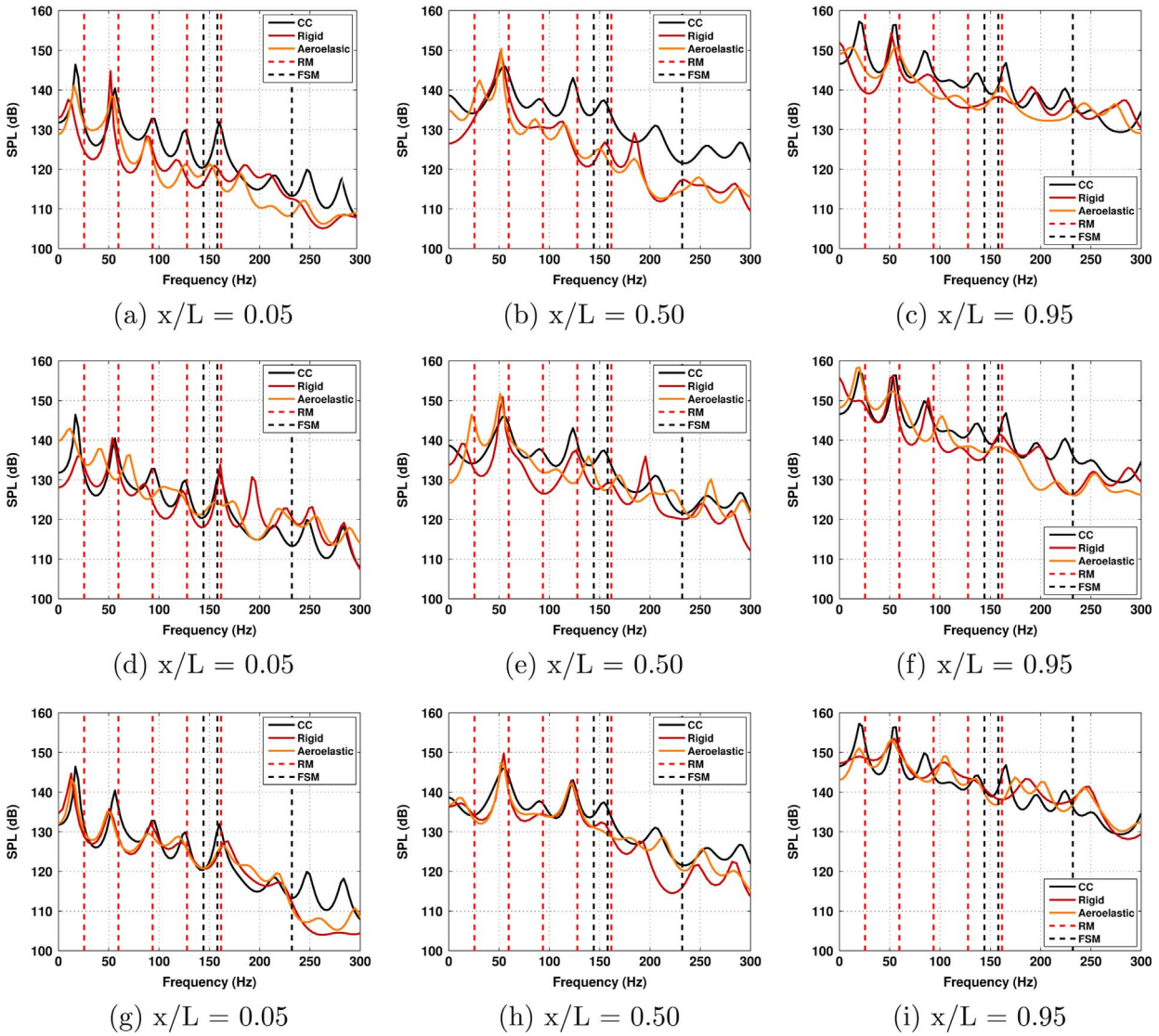

Fig. 11. PSD for the clean cavity comparing a store at carriage (a)–(c), at shear layer (d)–(f) and outside (g)–(i), and pressure (SPL) traces along the centerline on the cavity floor. RM – Rossiter modes and FSM - fin structural modes.

6.3. *Spectral content*

PSD plots for the front, middle and rear of the cavity for different positions of the store relative to the cavity are shown in Fig. 11 and compared with results from the clean cavity simulation.

Plots are compared against the first five Rossiter modes and first three fin structural modes (Table 1). Peaks were seen near the fin structural modes for the aeroelastic cases showing that the fins were deforming due to the presence of these frequencies in the fin loads. However, the aeroelasticity of the fins did not induce changes in the cavity noise as seen in the OASPL plots.

The general trend in the PSD spectra showed an increase in the SPL from the front wall to the aft wall and small reductions in higher frequency modes compared to those in the clean cavity. The broadband noise was reduced by the presence of the store, especially for the case at carriage position. This corresponded to a reduction in OASPL and BISPL levels for modes 1–4.

However, the amplitudes of some the cavity modes were higher with the presence of the store. At carriage, the amplitude of the second mode was higher at the front and at the middle of the cavity, while other modes were all reduced. When the store was at the shear layer and outside, the first and the second modes were stronger in the middle of the cavity. The combination of the lower broadband noise and the higher peak of the second mode leaded to fairly equivalent BISPL levels for the second mode with and without store. However, for the other modes, the decrease of broadband noise is higher than

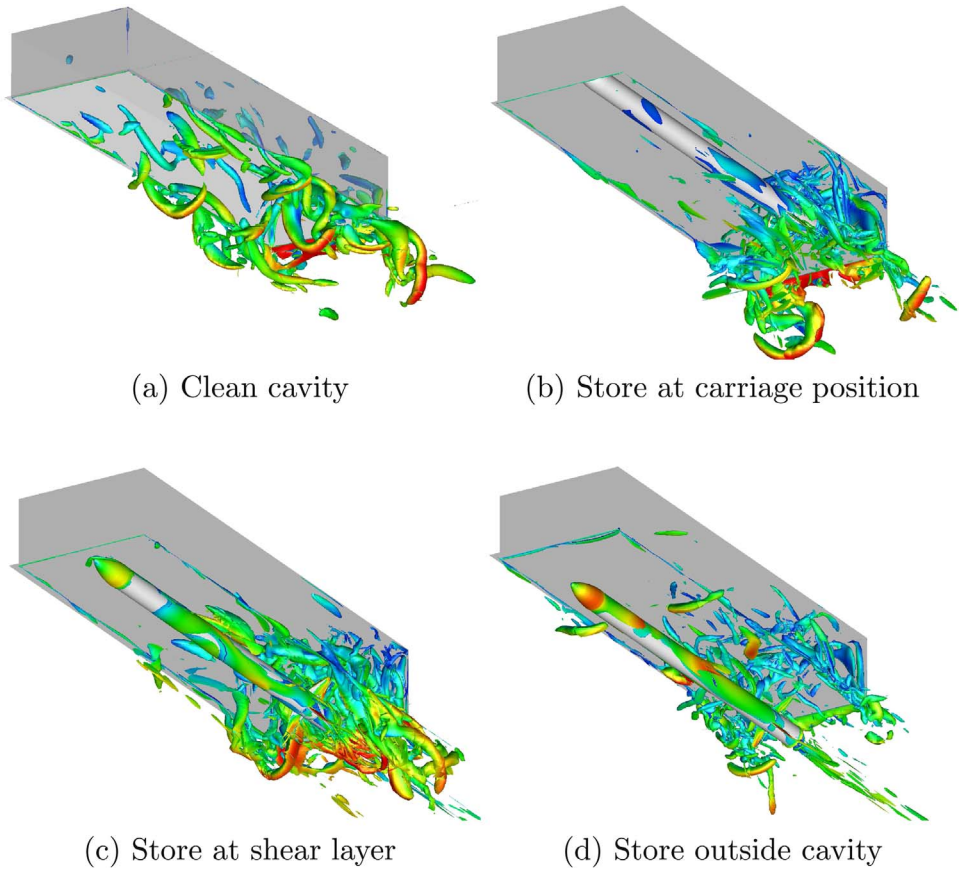

Fig. 12. Instantaneous iso-surfaces of Q-criteria for the clean $L/D=7$ cavity and the store at different positions relative to the cavity. Iso-surfaces at $Q=2000$ are shown colored with Mach number between 0.0 (blue) and 1.0 (red). (For interpretation of the references to color in this figure caption, the reader is referred to the web version of this paper.)

the increase of cavity modes peaks, so that the BISPL levels are decreasing. The PSD plots for the store outside the cavity showed similarities to the clean cavity as seen in the mean Mach number (Figs. 7(g) and (h)) and the OASPL (Figs. 11(g)–(i)). The flow retained most of the dominant frequencies seen in the clean cavity. The aeroelasticity shows negligible effect compared to the store position.

6.4. *Instantaneous flow-field*

In order to visualize structures, iso-surfaces of Q-criteria (Hunt et al., 1988) are presented in Fig. 12. The iso-surface values were chosen to highlight the high frequency structures that appeared after the shear layer breakdown and caused the broadband noise. Numerical Schlieren (Wu and Martin, 2007) contours are presented in Fig. 13 to highlight the coherence of the shear layer and its breakdown, between the clean cavity and the cavity and store configurations.

The clean cavity case shows a breakdown at 30% of cavity length and a large number of structures from the same point. At carriage position, structures were only seen towards the rear end of the cavity and the shear layer broke down on the second half of the cavity. This flow configuration is very different from the clean cavity case, and thus explains the low spillage seen on the mean Mach number slice in Fig. 7(c). When the store was positioned at the shear layer, few structures exist along the shear layer while the majority were confined to the rear end. The shear layer breakdown is earlier than for the carriage case. Outside the cavity, the store did not have much influence on the aft cavity region, creating less structural content in comparison to the other store positions but with more vortex shedding from the base of the store. Furthermore, the shear layer breakdown was seen at the fairly same point as the clean case.

The analysis of the sound pressure levels and the flow structure showed a large influence of the store position on the characteristics of the flow. The closer the store to the carriage position, the more coherent and quieter was the cavity. It was explained by a weaker cavity resonance and less broadband contents due to the later shear layer breakdown. This result is consistent with the experimental work of Wagner et al., 2014

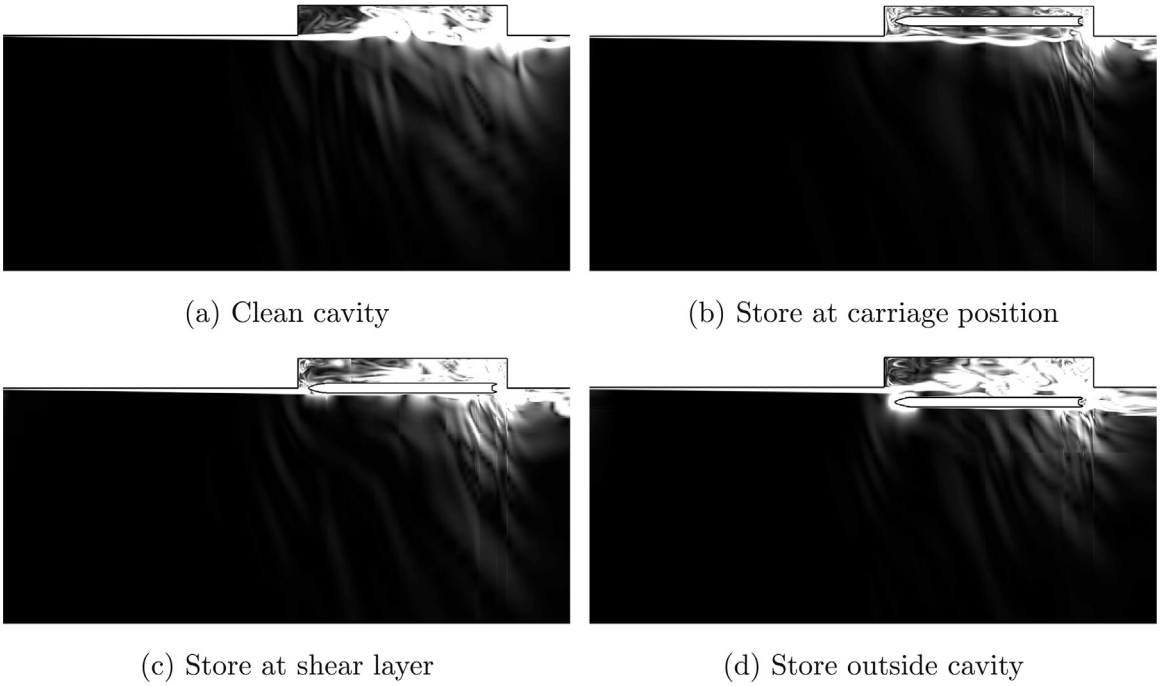

Fig. 13. Instantaneous contours of numerical Schlieren for the clean $L/D=7$ cavity and the store at different positions relative to the cavity. Planes are located at the centerline ($z/L = 0.0$) of the cavity.

6.5. Time-averaged forces and moments

6.5.1. Store loads

Time-averaged forces and moments acting on the store are shown in Fig. 14 for the body alone and the body plus fins. The forces and moments acting on each fins are shown in Figs. 15 and 16. This helps identify the contribution of the fins to the overall loads on the store.

For the carriage case, as the shear layer broke down on the second half of the cavity and reached a shallow depth of penetration, most of the store was shielded from the high dynamic pressure flow just outside the cavity. This explained the relatively low contribution of the axial force coefficient, C_X, as seen in Fig. 14(a). Moving the store outward of the cavity, the drag increased as the store is more influenced by the freestream and the flow reached larger depth of penetration with an earlier breakdown of the shear layer. The comparison of the force due to the body and due to the fins showed that the drag was mainly due to the body.

The transverse force coefficient on the body, C_Y, was always negligible as the store is placed at the centerline.

At carriage, the largest contribution in terms of forces to the body of the store was from C_Z, where the net effect on the store was a normal force. This force originated the larger recirculation in the cavity flow that dipped into the cavity on the aft half that retained the store into the cavity. This force was maximum at the shear layer and became negligible when the store was outside of the cavity.

The forces on the store did not show a noticeable effect of the aeroelasticity.

The rolling moment coefficient C_l on the store was negligible for all store positions as the resulting panel force on the four fins (Fig. 16) was close to zero. Similarly, the yawing moment C_n was negligible compared to the pitching moment.

The dominant moment on the store was the pitching moment C_m caused by the vertical force. The flow dips in the cavity with large velocity at the aft half and dips out at the front half with lower velocity. This leads to an imbalance of the forces along the store length that tends to move the store nose outwards of the cavity. As the vertical force, the pitching moment was maximum at the shear layer and became negligible when the store was outside of the cavity. The difference in the breakdown and shear layer depth of penetration also contributed to this change. Although not in the force coefficients, there was a noticeable difference between the flexible and the rigid fins. The C_m of the flexible fins was lower than the rigid fins by about 6.5%. This change may come from the fin deflection that modified the loads. The fins had a non-negligible contribution to the pitching moment of about 24%, as they were placed at about half missile length from the store gravity center and that the aft half experienced the larger vertical velocities.

Outside the cavity, the store only experienced a net axial force leading to negligible moments.

6.5.2. Fins loads

RMS values of the loads are represented by vertical black bars in the time-averaged forces and moments for each

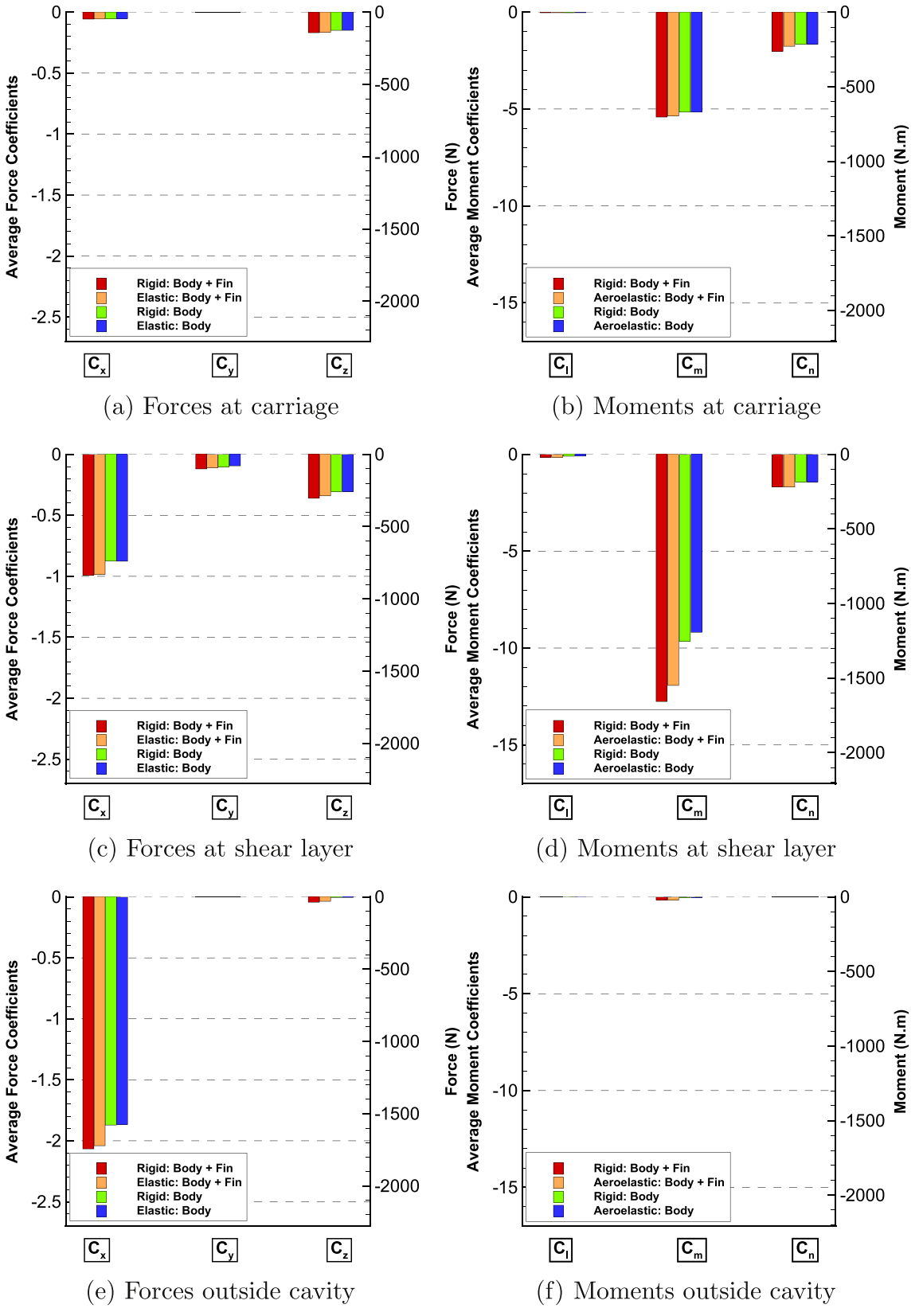

Fig. 14. Comparison of the time-averaged integrated force (a), (c), and (e) and moment (b), (c), and (d) coefficients acting on the store with and without fins.

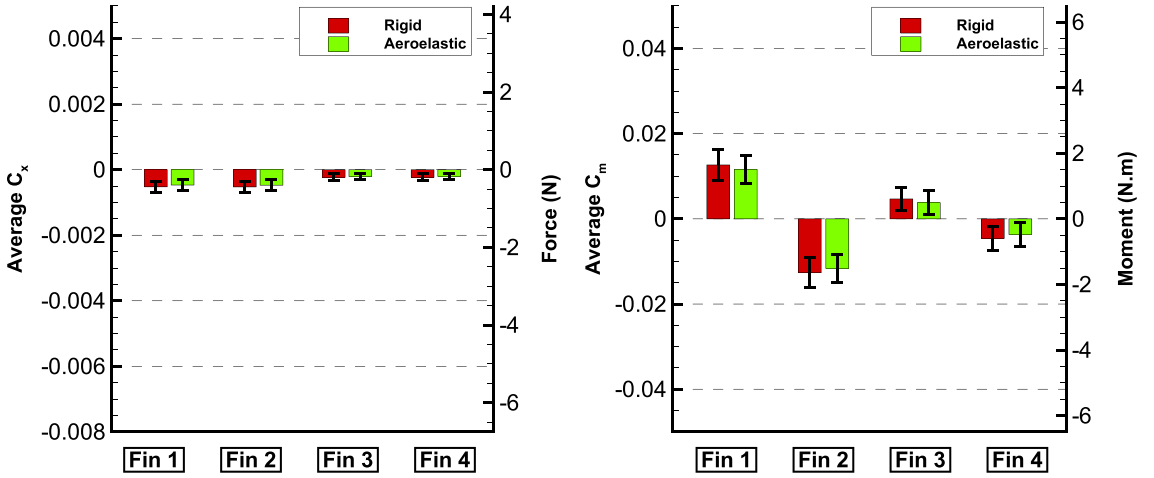

(a) Cx at carriage

(b) Cm at carriage

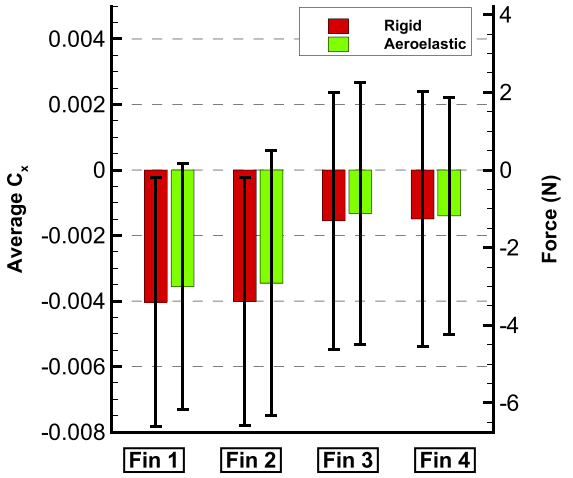

(c) Cx at shear layer

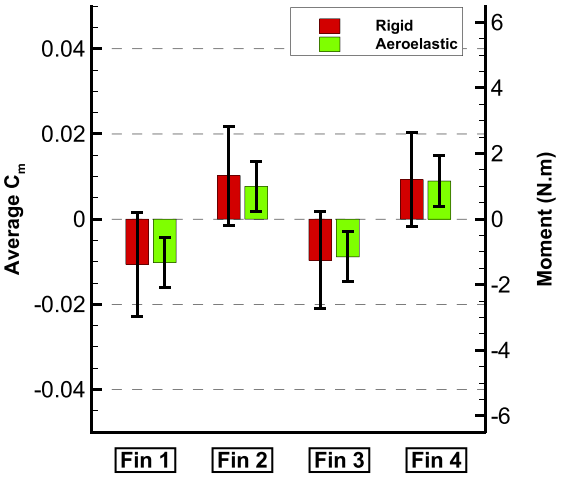

(d) Cm at shear layer

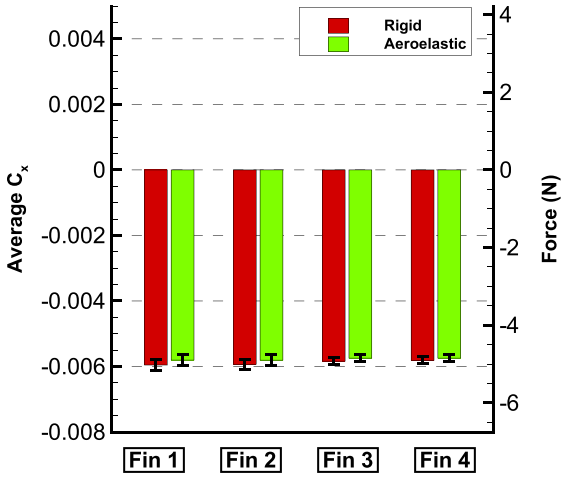

(e) Cx outside cavity

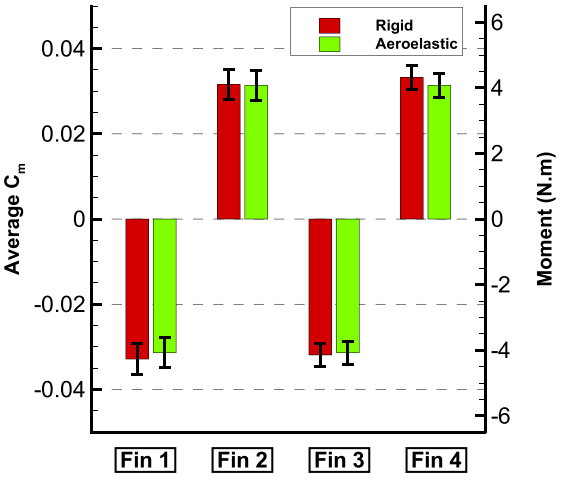

(f) Cm outside cavity

Fig. 15. Comparison of the time-averaged integrated drag and hinge moment coefficients acting on the fins.

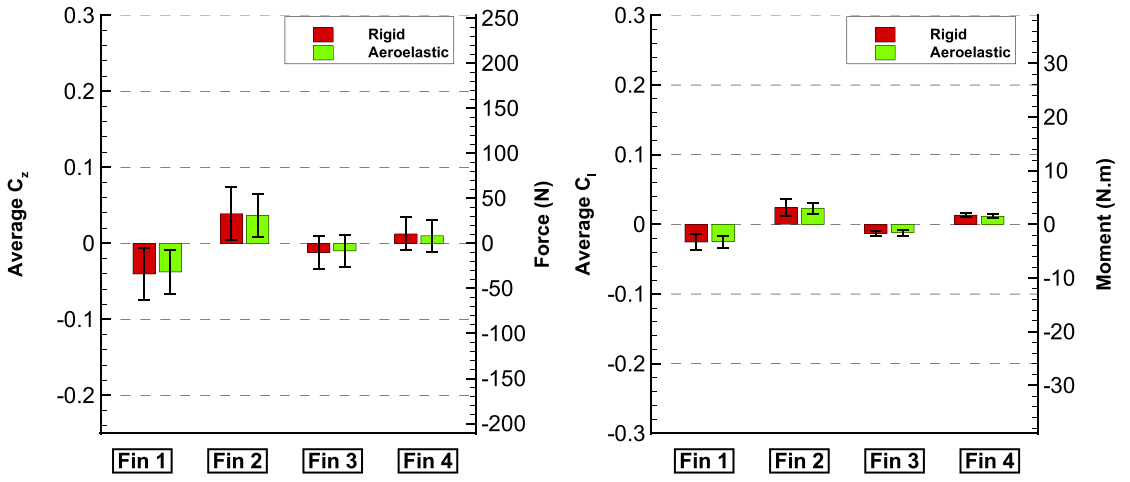

(a) Cz at carriage

(b) Cl at carriage

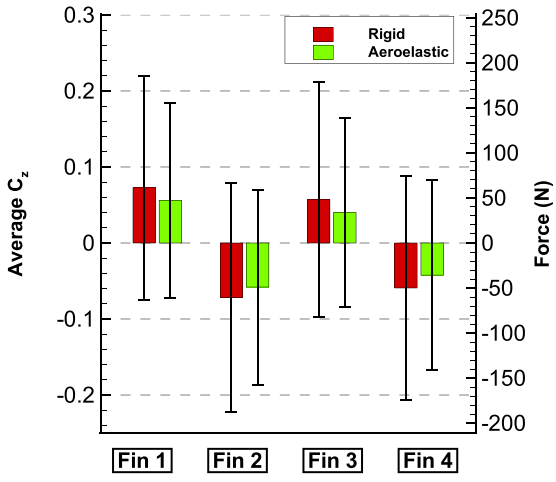

(c) Cz at shear layer

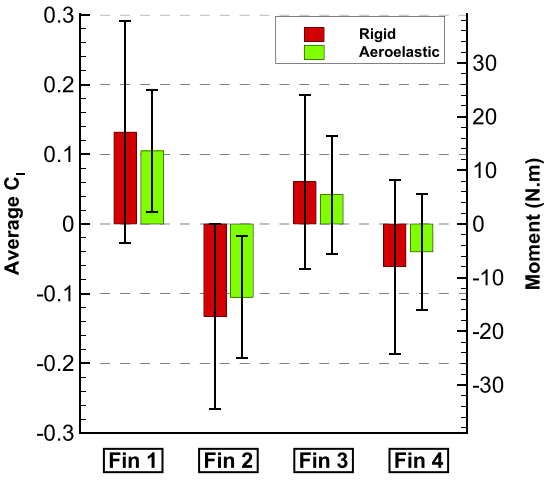

(d) Cl at shear layer

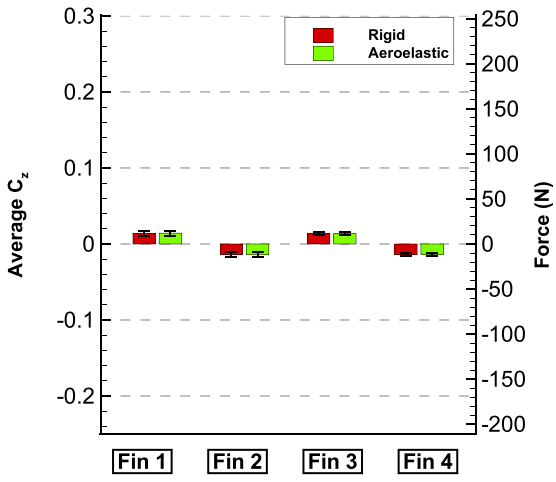

(e) Cz outside cavity

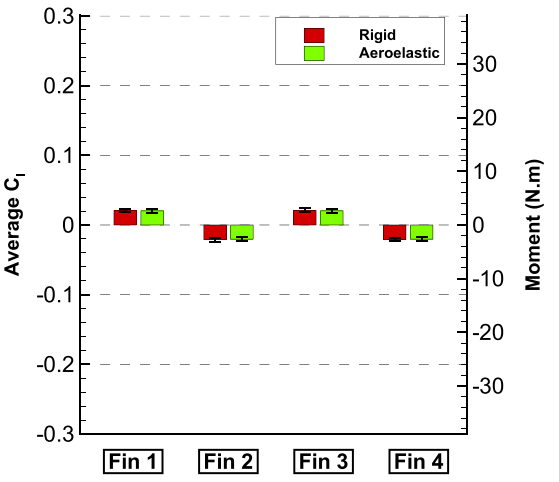

(f) Cl outside cavity

Fig. 16. Comparison of the time-averaged integrated panel force and bending moment coefficients acting on the fins.

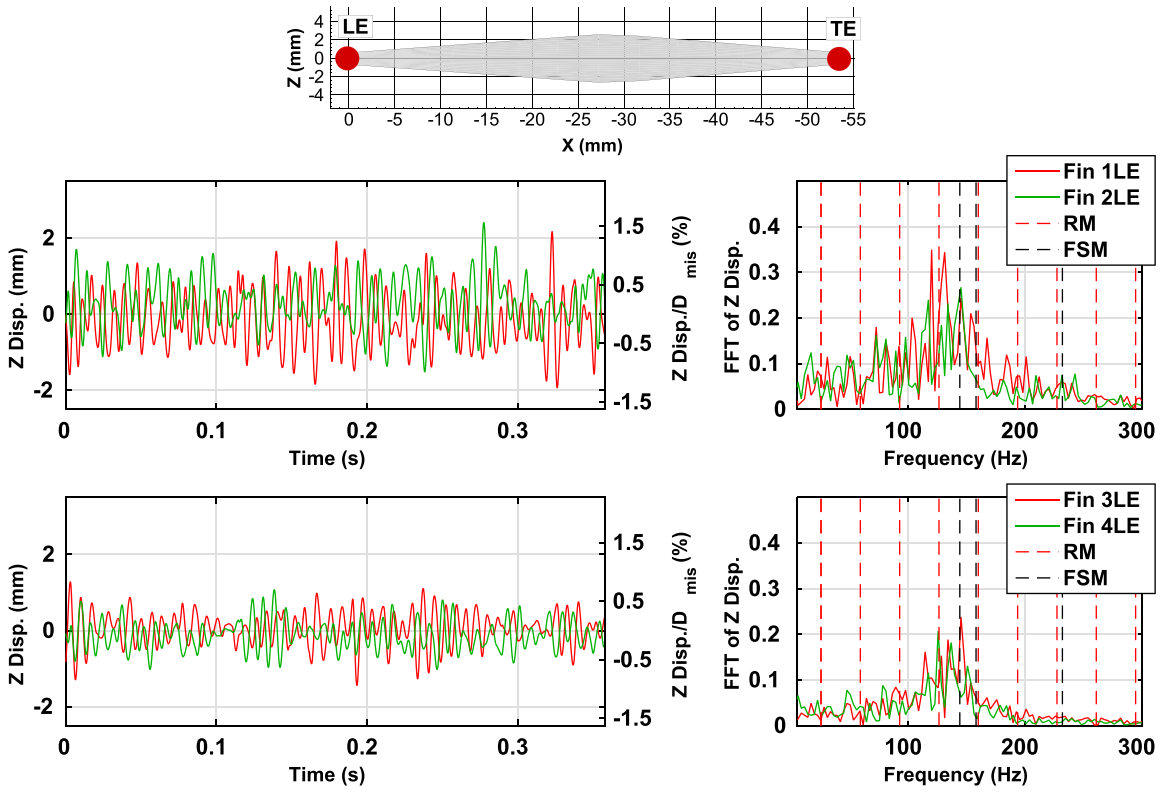

(a) Leading Edge Tip

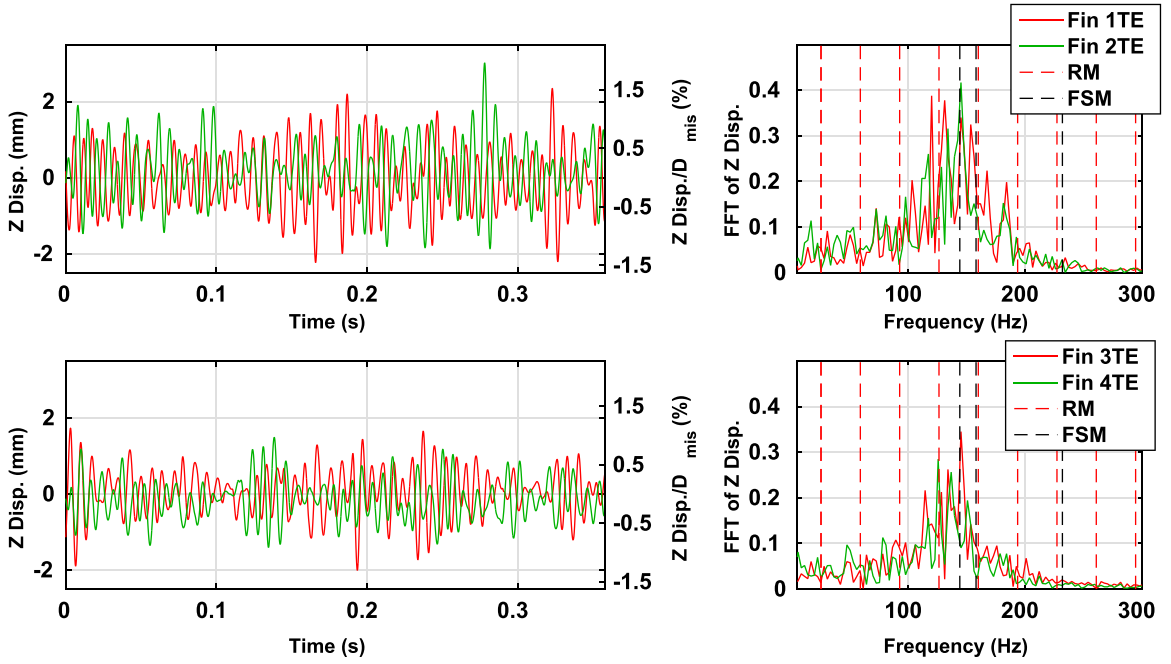

(b) Trailing Edge Tip

Fig. 17. FFT of the fin tip displacements compared against Rossiter modes with the fin structural frequencies for the store at shear layer. RM – Rossiter modes and FSM – fin structural modes.

individual fin shown in Figs. 15 and 16. The RMS values depend on the store position, and were maximum with the store at the shear layer directly experiencing the unsteadiness generated by the breakdown of the shear layer.

At carriage and at shear layer, while the contribution of the fins to the overall axial force coefficient acting on the store was negligible, it was interesting to note that fins three and four that were closer to the floor of the cavity were shielded further from the flow outside of the cavity, and had less than half the axial force coefficient than the fins closer to the shear layer.

Outside the cavity, all fins were driven by the freestream and experienced fairly identical loads and RMS.

6.6. Fin tip displacements

An analysis of the fin tip displacement was carried out to identify the correlation between the fin resonant frequencies and the cavity Rossiter modes. Fig. 17 presents the displacements of the leading and trailing edges of the fin tips and their FFTs for the store at the shear layer for which the most influence of the flexible fins was seen.

6.6.1. Store at carriage position

When the store was at carriage, the fins were not very active. Fins one and two that were closer to the shear layer were more active with deflections in the range of 0.3 mm (0.2% of D_{mis}) while fins three and four that were inside the cavity and were shielded from the high velocity flow were within the range of 0.2 mm (0.1% of D_{mis}). Arunajatesan et al. (2013) also found a maximum deflection of about 0.2% of his store diameter. The frequency content of the fin tip displacement was barely influenced by cavity modes and structural modes.

6.6.2. Store at cavity shear layer

The fins of the store had relatively large oscillations from the initial undeflected position (Fig. 17). For fins one and two the maximum deflections were in the range of 2.5 mm (1.6% of D_{mis}) while for fins three and four this range was lowered to 1.5 mm (1% of D_{mis}). This difference suggests that the internal part of the shear layer inside the cavity was less active than the external. The trailing edge experienced the larger displacement of 3 mm (1.9% of D_{mis}). The peaks in the FFT of the tip displacements were clustered around structural modes 1 and 2. The structural modes 3 and 4 were not seen to be excited by the flow that did not show sound pressure peaks at those frequencies (Fig. 11). Solely the cavity mode 4 excited the fin displacement leading to the dominant peak for fin 1 at the tip leading edge. At the trailing edge, the dominant peak appeared at the first structural mode for the fin 2. This case shows fluid dynamic forcing, but no evidence of mode matching.

7. Conclusions

The current paper presented aeroelastic computations for flexible fins of store in weapon bays idealized as rectangular cavities. This is the first time FSI was used in the context of cavity flows with stores and showed how the flow may induce vibrations in the fins. Detached-Eddy Simulations using the Spalart–Allamaras turbulence model was used to compute the flow in a cavity of length to depth ratio of 7 when a store was placed at the carriage position, at the cavity shear layer and at half-cavity depth outside the cavity. The influence of the cavity on the force and moment coefficients of the store was studied and the effect the store on the acoustics of the cavity was assessed. The root of the fin was free to move with a gap of 0.3% of the store diameter introduced between the root of the fin and the body of the store.

The closer the store to the carriage position, the more coherent and the quieter was the cavity proximity. It was explained by a weaker cavity resonance and less broadband contents due to a later shear layer breakdown. At the carriage position, the store was found to pacify the flow inside the cavity with a maximum reduction in OASPL of 7 dB towards the trailing edge of the cavity. The shear layer was affected along the length of the store with reductions in OASPLs seen to range from 1 to 4 dB. BISPLs showed that while the energy of other modes was reduced, mode 2 was still the dominant mode and retained its 'W' shape similar to the clean cavity. PSDs showed similar characteristics to the clean cavity. When the store was held outside the cavity, the flow topology and the noise field was similar to the clean case.

Average fin forces and moments were seen to be greater by a maximum of 50% for fins that were closer to the shear layer. The closer to the shear layer the fin, the higher its displacements and loads fluctuations. The aeroelastic loads were seen to be slightly lower than the rigid loads when the store was at the shear layer where the unsteadiness was the higher.

Fin tip displacements showed a maximum displacement of 1.6% of D_{mis} at shear layer and 0.2% of D_{mis} at carriage. The analysis of the spectral contents of the deflections showed that they were clustered around the first modal mode. The fourth cavity mode was also seen to excite the fins but no mode matching was evident.

In the future, efforts will be directed towards applying the aeroelastic method to the body of the store and studying the influence of the aeroelasticity on the separation characteristics of the store.

Acknowledgments

The financial support of the Engineering and Physical Sciences Research Council and MBDA Missile Systems through grant EP/C533380/1 is gratefully acknowledged. The use of the POLARIS HPC cluster of N8 and the Chadwick HPC cluster of the University of Liverpool is also gratefully acknowledged.

References

ANSYS, Documentation for ANSYS ICEM CFD v13 – User Manual ⟨www.academia.edu/3196257/ANSYS_ICEM_CFD_13_User_Manual⟩ (accessed 28.03.2014).
Arunajatesan, S., Bharadwaj, M., Riley, W.C., Ross, M., 2013. One-way coupled fluid structure simulations of stores in weapons bays. In: Proceedings of the 51st AIAA Aerospace Sciences Meeting Including the New Horizons Forum and Aerospace Exposition, Grapevine, Texas, USA. http://dx.doi.org/10.2514/6.2013-665.
Babu, S., Dehaeze, F., Barakos, G., 2014. Understanding the effect of stores in weapon bays using des and strongly-coupled aeroelastic simulations. In: 52nd Aerospace Sciences Meeting, AIAA SciTech, (AIAA 2014-1252). http://dx.doi.org/10.2514/6.2014-1252.
Barakos, G., Steijl, R., Badcock, K., Brocklehurst, A., 2005. Development of CFD capability for full helicopter engineering analysis. In: 31th European Rotorcraft Forum.
Childers, D., 1978. Modern Spectrum Analysis. IEEE Press, New York23–148 (Chapter 2).
Coley, C., 2011. An Investigation of Cavity Resonance and its Relationship to Store Force and Moment Loading (Ph.D. thesis). Air Force Institute of Technology, Wright-Patterson AFB, Department of Aeronautics And Astronautics (March).
Dehaeze, F., Barakos, G., 2012. Mesh deformation method for rotor flows. J. Aircr. 49 (1), 82–92.
Finney, L., 2010. Investigation of Cavity Flow Effects on Store Separation Trajectories. Trident Scholar Project Report No. 388 (Ph.D. thesis). U.S. Naval Academy (May).
Heller, H., Holmes, D., Covert, E., 1971. Flow-induced pressure oscillations in shallow cavities. J. Sound Vib. 18 (4), 545–553, http://dx.doi.org/10.1016/0022-460X(71)90105-2.
Hunt, J., Wray, A., Moin, P., 1988. Eddies, streams and convergence zones in turbulent flows. In: Proceedings of the Summer Program, Center for Turbulence Research, n89-24555, pp. 193–207.
Jameson, A., 1991. Time dependent calculations using multigrid, with applications to unsteady flows past airfoils and wings. In: Proceedings of the 10th AIAA Computational Fluid Dynamics Conference, Honolulu, Hawaii, USA, 24–26 June, AIAA-1991-1596.
Jarkowski, M., Woodgate, M., Barakos, G., Rokicki, J., 2014. Towards consistent hybrid overset mesh methods for rotorcraft CFD. Int. J. Numer. Methods Fluids 74 (8), 543–576, http://dx.doi.org/10.1002/fld.3861.
Larcheveque, L., Sagaut, P., Comte, P., 2004. Large-eddy simulation of a compressible flow in a three-dimensional open cavity at high Reynolds number. J. Fluid Mech. 516, 265–301.
Lawson, S., Barakos, G., 2010. Evaluation of des for weapons bays in UCAVs. Aerosp. Sci. Technol. 14 (6), 397–414, http://dx.doi.org/10.1016/j.ast.2010.04.006.
Lawson, S., Barakos, G., 2011. Review of numerical simulations for high-speed, turbulent cavity flows. Prog. Aerosp. Sci. 47 (3), 186–216, http://dx.doi.org/10.1016/j.paerosci.2010.11.002.
Lawson, S., 2009. High Performance Computing for High-Fidelity Multi-Disciplinary Analysis of Weapons Bays (Ph.D. thesis). University of Liverpool (October).
Lee, B., 2010. Effect of captive stores on internal weapons bay floor pressure distributions. J. Aircr. 47 (2), 732–735.
Leer, B.V., 1974. Towards the ultimate conservative difference scheme. II: monotonicity and conservation combined in a second order scheme. J. Comput. Phys. 14, 361–374.
M.S. Corporation. MSC Nastran 2005 Release Guide.
Nayyar, P., 2005. CFD Analysis of Transonic Turbulent Cavity Flows (Ph.D. thesis). University of Glasgow (August).
Nightingale, D., Ross, J., Foster, G., 2005. Cavity Unsteady Pressure Measurements – Examples from Wind-Tunnel Tests. Technical Report Version 3. Aerodynamics & Aeromechanics Systems Group, QinetiQ (November).
Osher, S., Chakravarthy, S., 1983. Upwind schemes and boundary conditions with applications to euler equations in general geometries. J. Comput. Phys. 50, 447–481.
Pierce, A., 1989. Acoustics: An Introduction to its Physical Principles and Applications. Acoustical Society of America, Woodbury, New York.
Roe, P., 1981. Approximate Riemann solvers, parameter vectors and difference schemes. J. Comput. Phys. 43, 357–372.
Rossiter, J.E., 1964. Wind Tunnel Experiments on the Flow Over Rectangular Cavities at Subsonic and Transonic Speeds. Technical Report 64037. Royal Aircraft Establishment (October).
Spalart, P., Allmaras, S., 1994. A one-equation turbulence model for aerodynamic flows. La Rech. Aerosp. 1, 5–21.
Taylor, N., 2011. Initial Aero and Structural Datapack (For Use in Accordance with GS31072009). Technical Report AERO/IRAD/11/M-034, MBDA.
van Albada, G., van Leer, B., Roberts, W., 1982. A comparative study of computational methods in cosmic gas dynamics. Astron. Astrophys. 108, 76–84.
Wagner, J., Casper, K., Beresh, S., Hunter, P., Spillers, R., Henfling, J., Mayes, R., 2015. Fluid-structure interactions in compressible cavity flows. Phys. Fluids 27 (6) http://dx.doi.org/10.1063/1.4922021.
Wagner, J., Beresh, S., Casper, K., Henfling, J., Spillers, R., Hunter, P., Mayes, R., 2013. Experimental investigation of fluid–structure interactions in compressible cavity flows. In: Proceedings of the 43rd Fluid Dynamics Conference, San Diego, California, USA. http://dx.doi.org/10.2514/6.2013-3172.
Wagner, J., Casper, K., Beresh, S., Hunter, P., Spillers, R., Henfling, J., 2015. Response of a store with tunable natural frequencies in compressible cavity flow, Sandia National Laboratories, American Institute of Aeronautics and Astronautics Inc., Albuquerque, NM 87185. http://dx.doi.org/10.2514/6.2015-1293.
Wu, M., Martin, M., 2007. Direct numerical simulation of supersonic turbulent boundary layer over a compression ramp. AIAA J. 45, 879–889, http://dx.doi.org/10.2514/1.27021.